

# Non-aligned Supervision for Real Image Dehazing

Junkai Fan, Fei Guo, Jianjun Qian, Xiang Li, Jun Li\* and Jian Yang\*

PCA Lab, Nanjing University of Science and Technology

{junkai.fan, feigu, csjqian, xiang.li.implus, junli, csjyang}@njjust.edu.cn \*corresponding author



Figure 1: Dehazing results on real-world images from CVPRws 2021 [22] and our Phone-Hazy. Our method can generate much clearer results compared to the state-of-the-art methods, DAD [49], RefineNet [68], CDD-GAN [4] and  $D^4$  [60].

## Abstract

Removing haze from real-world images is challenging due to unpredictable weather conditions, resulting in misaligned hazy and clear image pairs. In this paper, we propose a non-aligned supervision framework that consists of three networks - dehazing, airlight, and transmission. In particular, we explore a non-alignment setting by utilizing a clear reference image that is not aligned with the hazy input image to supervise the dehazing network through a multi-scale reference loss that compares the features of the two images. Our setting makes it easier to collect hazy/clear image pairs in real-world environments, even under conditions of misalignment and shift views. To demonstrate this, we have created a new hazy dataset called "Phone-Hazy", which was captured using mobile phones in both rural and urban areas. Additionally, we present a mean and variance self-attention network to model the infinite airlight using dark channel prior as position guidance, and employ a channel attention network to estimate the three-channel transmission. Experimental results show that our framework outperforms current state-of-the-art methods in the real-world image dehazing. Phone-Hazy and code will be available at [here](#).

## 1. Introduction

Hazy is a main restrictive factor to capturing a degraded image (e.g., limited visibility) during the imaging formation process, resulting in the poor performance of many computer vision applications, such as object detection [18], scene recognition [2], depth estimation [54], semantic segmentation [48] and autonomous driving [7]. Therefore, image dehazing, aiming to restore a clear image from a hazy input, has received more and more attention in the past decade [12, 5, 57, 69]. The hazing process is typically modeled as an atmospheric scattering model:

$$I(x) = J(x)t(x) + A_\infty(\lambda)(1 - t(x)), \quad (1)$$

where  $x$  represents the pixel position,  $I(x)$  is the input hazy image,  $J(x)$  is the restored scene radiance,  $A_\infty$  is the infinite airlight (the airlight radiance corresponding to an object at an infinite distance, e.g., the horizon),  $t(x) = e^{-\beta(\lambda)d(x)}$  is the transmission map,  $d(x)$  and  $\beta(\lambda)$  denote the scene depth and the scattering coefficient with the wavelength of light  $\lambda$ , respectively. Following this atmosphere scattering model, most deep learning methods for image dehazing can be broadly categorized into two groups: direct dehazing and indirect dehazing. Direct dehazing methods use aligned hazy/clear image pairs to train an end-to-end deep network in a supervised setting to produce the clear image. Indi-

rect dehazing methods use popular CNN-based networks, such as DCPDN [64] and BidNet [41], to estimate  $A_\infty$  and  $t(x)$  in order to restore the clear image using the atmospheric scattering model. Despite their promising results, these methods still face two challenges.

Firstly, most of the dehazing models are usually trained on the synthetic hazy/clear image pairs in an alignment setting, resulting in poor restorations on real-hazy images due to their domain gap. Although recent works [49, 63, 30, 62] try to reduce the gap using domain adaptation, the results are still not satisfactory as the data are sampled from different distributions (scenes). More importantly, it is impossible to collect a large number of the perfectly aligned hazy/clear image pairs from the real scene, because they are generally captured at different times, weather conditions and camera positions which result in pixel misalignment and shift views. Secondly, the popular networks often fail to predict the variations of  $A_\infty$  determined by the size of scattering particles and the wavelength of light in real-world [36, 70]. Also, they lack the useful physics priors to create the network structures, leading to inaccurate estimations and unsatisfied dehazing results.

To address these problems, we develop a non-aligned supervision framework, which consists of dehazing, infinite airlight, and transmission networks based on the atmosphere scattering model. One important idea is the use of non-aligned images to supervise the dehazing network. This use allows for clear images that are not perfectly aligned with the hazy images to be used for training. By relaxing the strict alignment constraint, it becomes easier to collect non-aligned image pairs from the same scene under more relaxed conditions. Furthermore, we propose a multi-scale reference loss that combines adversarial and contextual losses to optimize the dehazing network using multi-scale pairs. Another is to view  $A_\infty$  as a non-uniform map. To more effectively model the  $A_\infty$  present in hazy images, we present a mean and variance self-attention (mvSA) network. By incorporating both the dark channel prior (DCP) [19] and the hazy image, mvSA is able to highlight hazy features by computing their mean and predicting variations due to the effects of wavelength and scattering particles. Compared to DCP and self-attention (SA), our proposed mvSA network more accurately constrains the range of infinite airlight. Our contributions are summarized as follow:

- We propose a novel non-aligned supervision framework for dehazing real-world images. By using a non-aligned reference image to supervise the dehazing network, we can reduce the strict alignment requirements for hazy/clear image pairs. As far as we know, we are the first to investigate non-aligned supervision for single image dehazing in real-world scenarios.
- We present a mean and variance self-attention network

(mvSA) that utilizes the dark channel prior as position guidance to better model the infinite airlight. Our experimental results also confirm its effectiveness.

- We provide a real-world hazy dataset including 415 non-aligned hazy/clear image pairs, which are collected manually by using mobile phones in the different real scenes (*i.e.*, countryside and urban roads).

## 2. Related work

Here, we mainly review two categories: prior-based dehazing methods and learning-based dehazing methods.

**Prior-based methods** for haze removal rely on atmospheric scattering theory [36] and employ manually crafted priors based on empirical observations. These priors mainly include contrast maximization [52], dark channel prior (DCP) [19], color attenuation prior [72], color-line prior [15], and non-local prior [1]. Although effective in general, these methods may yield suboptimal results in complex real-world scenarios, particularly in sky regions where DCP struggles due to its reliance on priors that are specific to certain scenes and assumptions.

**Learning-based methods** use deep neural networks to learn either the parameters (*i.e.*, infinite airlight  $A_\infty$ , transmission map  $t(x)$  and hazy-free  $J(x)$ ) of the atmospheric scattering model or the mapping between hazy and clear images. For the former, many works [3, 45, 39, 64, 65, 28, 41, 42, 32] focused on directly estimating  $t(x)$  and  $A_\infty$  by using CNNs or GANs. Mondal *et al.* [39] proposed that airlight is non-uniform and defined it as  $A_\infty(\lambda)(1 - t(x))$ , while our infinite airlight only refers to  $A_\infty$ . Due to the difficulty of obtaining ground truths for  $t(x)$  and  $A_\infty$  in real scenes, these methods are difficult to achieve good results. To improve the accuracy of  $A_\infty$  and  $t(x)$ , some methods [35, 31, 58, 24] used an iterative optimization approach to obtain their optimal values, but with limited gains. The latter primarily rely on designing various network modules to efficiently extract features, without utilizing the atmospheric scattering model. Most of them [29, 44, 43, 8, 10, 13, 50] construct dehazing models using GAN variants as a basis and introduce perceptual loss [23] as a constraint. Part of these GAN variants mainly utilize multi-scale and attention mechanisms (*e.g.*, channel attention, spatial attention) to efficiently extract hazy features, such as [44, 43]. Besides, similar network architecture design ideas have also appeared in CNN-based dehazing networks [26, 64, 46, 11, 34, 12, 61]. Recently, visual transformers (ViT) is used to design different structures for improving dehazing performance [66, 51, 53, 17]. The aforementioned works mainly employ supervised learning methods that heavily rely on ground truth data, and are primarily trained on synthetic hazy (*i.e.*, SOTS [27], Cityscapes [9]). However, the dehazing effect is not ideal due to domain gaps and a lack of real hazy/clear image pairs.

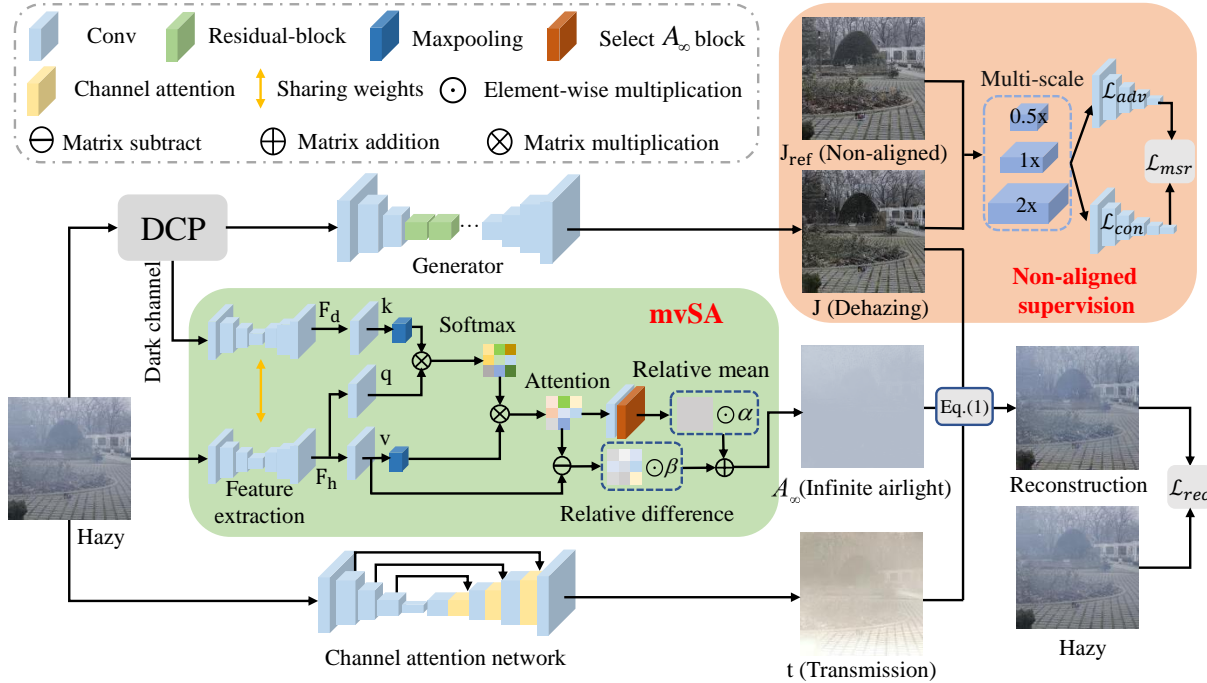


Figure 2: Overall pipeline of our non-aligned supervision framework with physical priors for the real image dehazing. It includes the mvSA and non-aligned supervision modules. mvSA can effectively estimate the infinite airlight  $A_\infty$  in real scenes. Our framework is different from the supervised dehazing models as it does not require aligned ground truths.

To address this issue, some works have proposed domain adaptive and unpaired dehazing models for real-world. These models are mainly built on the framework of CycleGAN [71], such as Cycle-Dehaze [14], DAD [49], and D<sup>4</sup>. Chen *et al.* [5] proposed a dehazing framework pre-trained on synthetic datasets and fine-tuned on real data with physical priors. Yang *et al.* [59] employed deep networks to estimate  $A_\infty$ ,  $t(x)$ , and  $J(x)$  separately for reconstructing hazy images, and constraint dehazing results by using unpaired hazy/clear images, similar works like [68]. Both of these approaches do not perform well in real-world scenarios, mainly because of differences in sample distributions. Compared to the domain adaptive and unpaired supervision, our non-aligned supervision is a stronger constraint.

Different from the above mentioned methods, Our method outperforms previous dehazing models by training on paired real hazy datasets and extracting effective features from non-aligned reference images. Furthermore, we have redefined the  $A_\infty$  (*i.e.*, non-uniform map) and proposed a novel network (mvSA) that more accurately estimates  $A_\infty$  in real-world scenarios.

### 3. Methodology

In this section, we propose non-aligned supervision with physics priors in Fig. 2 based on the atmospheric scattering model in Eq. (1) to construct three dehazing, airlight, and transmission networks from the input hazy image. Firstly, we explore a non-aligned supervision setting to train the

dehazing network using a clear and non-aligned reference image. Secondly, we construct a mean and variance self-attention network to predict the  $A_\infty$  by using dark channel prior [19]. Before showing them, we first give the architectures of the dehazing and transmission networks.

*The dehazing network* is to directly generate a haze-free image from the input hazy image. As shown in Fig. 2, we compute a rough haze-free image using the DCP method [19] and then put it into the dehazing network. Its architecture is a shared generator network. For more details, please refer to the generator of CycleGAN [71].

*The transmission network* is to produce a three-channel transmission map by employing a channel attention network from the input hazy image in Fig. 2. Its architecture is an encoder-decoder structure [47] with skip connection across the feature scales. The final transmission map can be obtained by the guided filter [19].

We denote  $I \in \mathbb{R}^{3 \times H \times W}$  by the input hazy image,  $J_{\text{ref}} \in \mathbb{R}^{3 \times H \times W}$  by the reference image,  $J \in \mathbb{R}^{3 \times H \times W}$  by the output of the dehazing network with the input  $I$ ,  $t \in \mathbb{R}^{3 \times H \times W}$  by the output of the transmission network. Note that  $J_{\text{ref}}$  is not aligned to  $I$  or  $J$ .

#### 3.1. Non-aligned Supervision

Here, our key idea is that we use a clear and non-aligned reference image  $J_{\text{ref}}$  to supervise the dehazing network. We formulate the non-aligned supervision setting as a multi-scale reference loss between  $J_{\text{ref}}$  and  $J$ . This loss is to han-

dle the learning problem of pixel misalignment by calculating their feature similarity.

**Multi-scale reference loss** between  $J_{\text{ref}}$  and  $J$  includes a multi-scale adversarial loss and a multi-scale contextual loss. Both  $J_{\text{ref}}$  and  $J$  are augmented using the same three scales (*i.e.*,  $0.5\times$ ,  $1\times$  and  $2\times$ ). In this paper, they are denoted by  $\mathbf{J}_{\text{ref}} = \{J_{\text{ref}}^i\}_{i=1,2,3}$  and  $\mathbf{J} = \{J^i\}_{i=1,2,3}$ . Mathematically, The multi-scale reference loss is described as  $\mathcal{L}_{\text{msr}}(\mathbf{J}_{\text{ref}}, \mathbf{J}) =$

$$\omega_1 \mathcal{L}_{\text{msr-adv}}(\mathbf{J}_{\text{ref}}, \mathbf{J}) + \omega_2 \mathcal{L}_{\text{msr-con}}(\mathbf{J}_{\text{ref}}, \mathbf{J}), \quad (2)$$

where  $\omega_1$  and  $\omega_2$  are positive hyper-parameters to balance the two losses. They are set to 1 by default in this paper.

**Multi-scale adversarial loss.** Since the adversarial learning [16] has a strong ability to generate realistic images very well, this work is to employ the adversarial loss to supervise the dehazing network (generator) and a discriminator network. The discriminator network is a simple CNN with 5 layers and applies a convolution to produce a one-dimensional output. All layers use  $4 \times 4$  Convolution-BatchNorm-LeakyReLU layers with stride 2, except that the first and last layers do not use the BatchNorm. Furthermore, we extend the adversarial loss to a multi-scale adversarial loss:  $\mathcal{L}_{\text{msr-adv}}(\mathbf{J}_{\text{ref}}, \mathbf{J}) =$

$$\sum_{i=1}^3 \mathcal{L}_{\text{msr-adv}}(J_{\text{ref}}^i, J^i) = \sum_{i=1}^3 \mathbb{E}_{J_{\text{ref}}^i} [\log D(J_{\text{ref}}^i)] + \mathbb{E}_{J^i} [\log(1 - D(J^i))], \quad (3)$$

where  $i$  represents the different scales, and  $J$  is generated by the dehazing network so that it is trained by using the above loss.

**Multi-scale contextual loss.** To better explore the unaligned and clear reference image, we are inspired by the contextual loss [37] which aims to compute the cosine similar distance between the unaligned images for image-to-image translation tasks. We extend it to a multi-scale contextual loss, which is defined as  $\mathcal{L}_{\text{msr-con}}(\mathbf{J}_{\text{ref}}, \mathbf{J}) =$

$$\sum_{i=1}^3 \mathcal{L}_{\text{msr-con}}(J_{\text{ref}}^i, J^i) = \sum_{i=1}^3 \sum_{l=1}^3 -\log [S(\Phi^l(J^i), \Phi^l(J_{\text{ref}}^i))], \quad (4)$$

where  $S$  is the contextual similarity between image features, and  $\Phi^l(J)$  and  $\Phi^l(J_{\text{ref}})$  represent the feature maps extracted from layer  $l$  of the VGG-16 network  $\Phi$  with the inputs  $J$  and  $J_{\text{ref}}$ , respectively.

Our non-aligned supervision brings an important benefit to relaxing the strict alignment requirement on the hazy/clear image pair. This leads us to easily collect the non-aligned hazy/clear image pairs in the same real scenes under some relaxed conditions, *e.g.*, pixel misalignment, and shift views. Moreover, we use mobile phones to build a real-world hazy dataset (termed Phone-Hazy).

### 3.2. Mean and Variance Self-attention

In this subsection, we introduce a mean and variance self-attention (mvSA) network to better model the infinite airlight  $A_\infty$  by fusing the useful DCP prior [19] to find the high-quality infinite airlight from an input hazy image  $I$ . The dark channel map  $D$  of  $I$  is computed by the DCP method [19]. We employ a shared network to extract features of  $D$  and  $I$ , and put them into our mvSA network for estimating a better  $A_\infty$  in Fig. 2.

**The shared network** is an encoder-decoder structure with skip connection across the feature scales [47] (*its structure is provided in supplemental material*). It is used to extract the features of the dark channel image  $D$  and the haze image  $I$ , denoted by  $F_d \in \mathbb{R}^{B \times C \times H \times W}$  and  $F_h \in \mathbb{R}^{B \times C \times H \times W}$ , where  $B$ ,  $C$ ,  $H$  and  $W$  are the batch size, channel, height, and weight, respectively.

**The mvSA network** is a mean and variance self-attention to estimate the infinite airlight  $A_\infty$  by using the dark channel prior as position guidance. It employs the self-attention [55] to highlight the hazy region of the dark channel feature  $F_d$  and the hazy feature  $F_h$ , takes the mean of the top 1% brightest pixels of the hazy region as the mean of  $A_\infty$ , and designs the difference between the hazy feature and the self-attention feature to predict the variance of  $A_\infty$ . The mvSA network is mathematically described as follows.

Following the features  $F_d$  and  $F_h$  extracted by the above shared network, we transform them to compute the embedding query  $q_h$ , key  $k_d$  and value  $v_h$  by using convolutional operations with the kernel size  $1 \times 1$ , denoted by  $C_h^q$ ,  $C_d^k$  and  $C_h^v$ , respectively. These embeddings are described as

$$q_h = C_h^q(F_h), \quad k_d = C_d^k(F_d), \quad v_h = C_h^v(F_h), \quad (5)$$

where  $q_h \in \mathbb{R}^{B \times \frac{C}{8} \times H \times W}$ ,  $k_d \in \mathbb{R}^{B \times \frac{C}{8} \times H \times W}$  and  $v_h \in \mathbb{R}^{B \times \frac{C}{8} \times H \times W}$ . To reduce the computational cost,  $k_d$  and  $v_h$  are down-sampled by  $4 \times 4$  maxpooling operation, denoted by  $\mathcal{M}$ . They are defined as

$$\hat{k}_d = \mathcal{M}(k_d), \quad \hat{v}_h = \mathcal{M}(v_h), \quad (6)$$

where  $\hat{k}_d \in \mathbb{R}^{B \times \frac{C}{8} \times \frac{H}{4} \times \frac{W}{4}}$  and  $\hat{v}_h \in \mathbb{R}^{B \times \frac{C}{8} \times \frac{H}{4} \times \frac{W}{4}}$ . The attention weight is calculated by matrix multiplication between the reshaped  $q_h \in \mathbb{R}^{B \times (HW) \times \frac{C}{8}}$  and the reshaped  $\hat{k}_d \in \mathbb{R}^{B \times \frac{C}{8} \times \frac{HW}{16}}$  followed with the activation of softmax. Then, the attention map  $F_{\text{att}} \in \mathbb{R}^{B \times \frac{C}{8} \times HW}$  is obtained by multiplying the attention weight and the reshaped  $\hat{v}_h \in \mathbb{R}^{B \times \frac{HW}{16} \times \frac{C}{8}}$ , which is written as:

$$F_{\text{att}} = \text{softmax}(\hat{k}_d \otimes q_h) \otimes \hat{v}_h, \quad (7)$$

where  $\otimes$  represents matrix multiplication. Based on the reshaped attention map  $F_{\text{att}} \in \mathbb{R}^{B \times \frac{C}{8} \times HW}$  and the embedding  $v_h$ , the mean and variance of the infinite airlight

Data Settings	Methods	Real-world Smoke				Phone-Hazy		RTTS (Only testing)			Params (M)	Reference
		PSNR $\uparrow$	SSIM $\uparrow$	FADE $\downarrow$	NIQE $\downarrow$	FADE $\downarrow$	NIQE $\downarrow$	FADE $\downarrow$	NIQE $\downarrow$	Votes $\uparrow$		
Unpaired	DCP [20]	15.01	0.39	0.3961	4.1303	0.8235	5.4222	0.7846	6.0006	-	-	CVPR'09
	DisentGAN [59]	14.93	0.27	0.7081	5.5187	0.9235	5.1244	1.2620	6.1112	-	11.48	AAAI'18
	RefineNet [68]	15.44	0.42	0.3042	4.1840	1.0889	4.9251	0.9145	5.6594	137	11.38	TIP'21
	CDD-GAN [4]	12.16	0.25	0.3174	5.3888	0.8147	3.9248	0.7792	4.9035	83	29.27	ECCV'22
	D <sup>4</sup> [60]	14.28	0.76	0.6903	4.9969	1.2064	6.7865	1.2227	7.9228	42	<b>10.70</b>	CVPR'22
Paired	DAD [49]	16.12	0.53	1.1008	5.5886	1.1837	5.7004	1.2937	7.0237	-	54.59	CVPR'20
	PSD [5]	12.86	0.44	1.1304	4.4485	1.4651	4.5386	1.1578	5.7828	83	33.11	CVPR'21
Non-aligned	<b>NSDNet (Ours)</b>	<b>19.92</b>	<b>0.78</b>	<b>0.3031</b>	<b>3.7686</b>	<b>0.7621</b>	<b>3.7884</b>	<b>0.7419</b>	<b>3.6905</b>	<b>605</b>	11.38	-

Table 1: Quantitative results on three real-world smoke/hazy datasets.  $\downarrow$  denotes the lower the better.  $\uparrow$  denotes the higher the better. Note that we only selected the latest dehazing methods (*i.e.*, RefineNet, CDD-GAN, D<sup>4</sup> and PSD) for the user study.

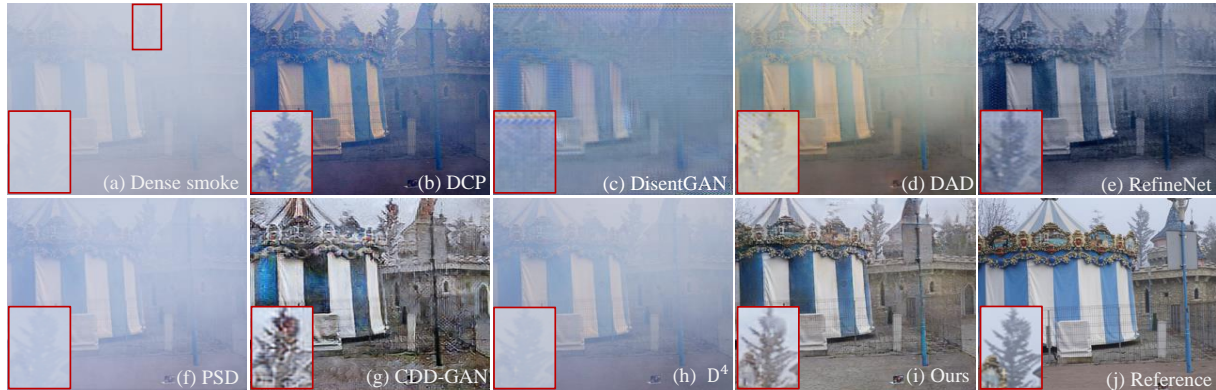


Figure 3: Example results on the real-world smoke dataset. Our method can remove smoke and generate images visually closer to the non-aligned reference. The red box corresponds to the zoomed-in patch for better comparison.

$A_\infty \in \mathbb{R}^{B \times 3 \times H \times W}$  is computed by

$$A_\infty = \alpha A_m + \mu A_v, \quad (8)$$

$$A_v = C_{1 \times 1}(|v_h - F_{\text{att}}|), \quad (9)$$

$$A_m = U_{A_\infty}[C_{1 \times 1}(F_{\text{att}})], \quad (10)$$

where  $A_m \in \mathbb{R}^{B \times 3 \times H \times W}$  and  $A_v \in \mathbb{R}^{B \times 3 \times H \times W}$  are the relative mean and relative variation, respectively.  $\alpha$  and  $\mu$  are the adjustment factors of the corresponding terms.  $C_{1 \times 1}(\cdot)$  is a convolutional operation with  $1 \times 1$  filter to reduce the channels,  $U_{A_\infty}[\cdot]$  represents the  $A_\infty$  selection from attention feature map.

Note that our mvSA is a more general and better form to estimate the mean and variance maps of the infinite airlight in real scenes compared to the previous works [19, 64, 28, 35, 68, 5] which only consider the limited three-channel constants, failing modeling the variation.

### 3.3. Training Loss

Finally, the training loss function is described as follow:

$$\mathcal{L}_{\text{all}} = \mathcal{L}_{\text{msr}} + \mathcal{L}_{\text{rec}}, \quad (11)$$

where  $\mathcal{L}_{\text{msr}}$  is the multi-scale reference loss in Eq. (2), and  $\mathcal{L}_{\text{rec}}$  is the reconstruction loss. Based on the atmosphere scattering model in (1),  $\mathcal{L}_{\text{rec}}$  is defined as:  $\mathcal{L}_{\text{rec}}(I_{\text{rec}}, I) =$

$$\theta \mathcal{L}_{\ell_1}(I_{\text{rec}}, I) + \gamma \mathcal{L}_p(I_{\text{rec}}, I) + \eta \mathcal{L}_{\text{ssim}}(I_{\text{rec}}, I), \quad (12)$$

where  $\mathcal{L}_{\ell_1}$  is the mean absolute difference loss,  $\mathcal{L}_p$  denotes the perceptual loss [23],  $\mathcal{L}_{\text{ssim}}$  represents the structural similarity (SSIM) loss [56].  $\theta$ ,  $\gamma$  and  $\eta$  are the weight coefficients of the corresponding items, respectively. In addition, the reconstruction loss can not only supervise the training of infinite airlight, transmission, and dehazing networks but also keep the features of dehazing results independent of the non-aligned reference image.

## 4. Experiments

We conduct experiments on three real-world smoke and hazy datasets to verify the effectiveness of the proposed method by comparing it with the state-of-the-art single-image dehazing methods. We also conduct an ablation study to justify the effectiveness of the core modules of the proposed method. *Note that synthetic experiments, Phone-Hazy dataset details, more visual results, and more quantitative comparisons are provided in supplementary material.*

### 4.1. Experimental Settings

**Real-world smoke/hazy Datasets.** *The Real-world smoke dataset* is collected from the 2018-2021 CVPR workshops dehazing challenge, which includes I-HAZE, O-HAZE, and NH-HAZE. It contains 155 pairs of smoke and clear images of real indoor and outdoor scenes, and these smoke images consist of homogeneous and non-



Figure 4: Comparison of dehazing results on the real-world Phone-Hazy dataset. Our method can remove hazy and generate images which are visually closer to the non-aligned reference image.

homogeneous smoke. Besides, we resize the image of the datasets to  $286 \times 286$ , and then randomly crop images to  $256 \times 256$ , so that the data pairs are unaligned. We randomly select 147 images for training and the remaining 8 images for the test, where the training images and test images do not overlap.

*Two real-world hazy datasets.* One is a *Phone-Hazy* that we use mobile phones (e.g., iPhone XR) to capture non-aligned image pairs on hazy/clear days in the same place for building a real-world hazy dataset. To enrich the diversity of the hazy scenes, we collect dense hazy in the countryside and urban roads. There have a total of 415 pairs of hazy and clear images of outdoor scenes, of which 375 images were used for training and the remaining 40 images for the test. The image patch size used in the training process is set to be  $256 \times 256$  pixels. Another is the *RTTS dataset*. RTTS is a real-world hazy dataset for outdoor scenes from the RESIDE dataset [27]. In this work, RTTS is a third-party dataset that was only used to test the dehazing methods, which contains 4322 real hazy images and does not have corresponding ground truths.

**Implementation details.** Firstly, in the reconstruction loss, the corresponding weight parameters  $\theta$ ,  $\beta$ , and  $\eta$  of  $\ell_1$  loss, perceptual loss, and SSIM loss are set to 5, 1, and 1, respectively. The default value for  $\omega_1$  and  $\omega_2$  in Eq. (2) are set to 1. Secondly, in Eq. (8), we set the relative mean  $\alpha$  and relative variance  $\beta$  to be 1.2 and  $0.25 \times 10^{-3}$ . In training processing, we use ADAM [25] optimizer with an initial learning rate of  $2 \times 10^{-4}$ . Our model was trained for 400 epochs by Pytorch with three NVIDIA GeForce RTX TITAN GPUs.

**Evaluations.** In this work, we use Fog Aware Density Evaluator (FADE) [6], Natural Image Quality Evaluator (NIQE)

[38] to evaluate the dehazing results without the ground truths (GT). In addition, we also employ PSNR [21] and SSIM [56] to evaluate the dehazing results with the GT.

## 4.2. Results on real smoke/hazy datasets

To evaluate the generalization and effectiveness of our NSDNet on real smoke and hazy scenes, we compare with some state-of-the-art (SOTA) methods including DCP [19], DisentGAN [59], DAD [49], RefineNet [68], PSD [5], CDD-GAN [4] and  $D^4$  [60]. For fair comparisons with these SOTA methods, we fine-tune them using our collected training datasets to achieve their best performance.

*Results on the real-world smoke dataset.* Table 1 summarizes the results of the quantitative comparison, and our NSDNet achieves the best PSNR, SSIM, FADE, and NIQE, which are much higher than all the SOTA methods. Furthermore, Fig. 3 shows the visual restoration results of the smoke image. Compared to the SOTA methods, we can see that our NSDNet is closer to the clear reference image from colors and textures. These methods usually fail to remove the smoke since they lack the constraints of physical priors and design the models for the synthetic dataset. For example, DCP and RefineNet produce a darker dehazing result and still retain a small amount of smoke, while DisentGAN, DAD, PSD, and  $D^4$  don't remove heavy smoke very well. In addition, CDD-GAN generates a more blurry texture and suffers from color distortion.

*Results on the real-world Phone-Hazy dataset collected by us.* Fig. 4 showcases the dehazing visualizations. Overall, the dehazing results reveal that our NSDNet has better brightness and texture details than the other SOTA methods. In particular, DCP suffers from serious color distortions.

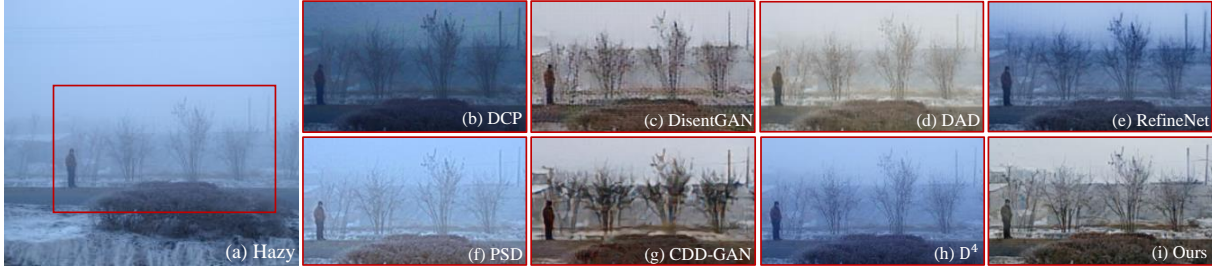


Figure 5: Results on RTTS dataset. Our method can remove hazy in far distance and restore more details.



Figure 6: Effectiveness of  $mvSA$  and  $\mathcal{L}_{msr}$  on a real dense hazy image with long-range view (*challenging scene*).

Ablations for core module	Phone-Hazy		Real-world Smoke			
	FADE↓	NIQE↓	FADE	NIQE	PSNR↑	SSIM↑
Baseline	0.8623	5.1218	0.3512	3.9455	16.48	0.55
+mvSA	0.8387	4.7817	0.3403	3.9087	17.01	0.57
+mvSA+ $\mathcal{L}_{msr}$	<b>0.7621</b>	<b>3.7884</b>	<b>0.3031</b>	<b>3.7686</b>	<b>19.92</b>	<b>0.78</b>

Table 2: Quantitative results of ablation study on real-world smoke and Phone-Hazy dataset.

DisentGAN, DAD, RefineNet, and  $D^4$  have some remaining haze artifacts, respectively. Moreover, although PSD brightens the scene, it does not remove the hazy. Even if CDD-GAN shows good dehazing ability, the texture, and color of its dehazing result are unsatisfactory in detail. In general, our NSDNet can restore more details and obtain visually pleasing images, especially for the brightness restoration of scenes. Due to no aligned ground truths, in addition, Table 1 reports the NIQE and FADE results. We can see that our NSDNet obtains the lowest NIQE and FADE values, demonstrating its excellent performance.

*Results on the real-world RTTS dataset.* To further verify the generalization ability of our NSDNet, all methods only test on the RTTS dataset. Their quantitative comparisons are reported in Table 1. We can see that our NSDNet obtains the lowest NIQE and FADE values, while also gets a much better *user study*, demonstrating its restoration power of real image dehazing. Besides, some visual comparisons are shown in Fig. 5 and we have the following observations: 1) RefineNet, PSD and  $D^4$  cannot remove hazy well in the far distance, 2) CDD-GAN restores the images with unsatisfactory texture and color though it is visually close to our NSDNet, and 3) in contrast, our NSDNet not only removes hazy but also restores the brightness and texture details.

### 4.3. Ablation Study

**Effect of  $mvSA$  and  $\mathcal{L}_{msr}$ .** To verify the effectiveness of the  $mvSA$  network and the multi-scale reference loss  $\mathcal{L}_{msr}$ ,

we design a series of ablations to analyze our method on real-world smoke and Phone-Hazy datasets. A *baseline* of the dehazing framework is constructed by using two deep networks for clear scenes  $J$  and transmission map  $t$ , and a constant infinite airlight produced by a deep network (*i.e.*, U-Net). It is trained by using the reconstruction loss. We use the  $mvSA$  network instead of the DCP method and add  $\mathcal{L}_{msr}$  to train the dehazing network in the baseline as *baseline+mvSA* and *baseline+mvSA+ $\mathcal{L}_{msr}$*  (Our NSDNet). The quantitative results are reported in Table 2. It can see that *baseline+mvSA+ $\mathcal{L}_{msr}$*  gets the lowest FADE and NIQE values, demonstrating that our method achieves an excellent performance of real image dehazing.

Furthermore, Fig. 6 shows the dehazing visualizations of a challenging hazy image with a long-range view. *baseline* contains color distortion and still has many haze residuals due to the inaccurate estimate of the infinite airlight ( $A_\infty$ ). In contrast, *baseline+mvSA* can recover a better scene than *baseline* as shown in (c) because  $mvSA$  estimates effectively the variation of the infinite airlight. More importantly, (d) shows that *baseline+mvSA+ $\mathcal{L}_{msr}$*  can produce clearer and more pleasing dehazing results (*e.g.*, the texture of the sky area and far buildings) than *baseline+mvSA*. This verifies the effectiveness of  $\mathcal{L}_{msr}$ .

To further verify that  $mvSA$  is able to learn better infinite airlight  $A_\infty$ , we also visualize it using a real smoke image compared to the popular DCP method with a constant infinite airlight in Fig. 7. Following the varying smokes (a), the infinite airlight  $A_\infty$  (b) predicted by  $mvSA$  can model its more realistic variation in comparison with the DCP method (f). Furthermore, compared (d) with (h), our  $A_\infty$  and  $t$  can generate a much better dehazing result using the Eq. (1). Additionally, we visualize the attention map depending on the dark channel prior and the hazy image in Fig. 7 (e). The attention area is just over the location of heavy haze, showing the effectiveness of the  $mvSA$  network.

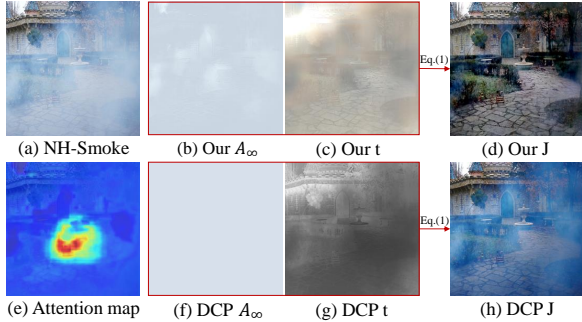


Figure 7: Visualizations of the dehazing result  $J$ , the infinite airlight  $A_\infty$ , the attention map and the transmission map  $t$ .

Misalignment	scale	PSNR $\uparrow$	SSIM $\uparrow$	FADE $\downarrow$	NIQE $\downarrow$
0 pixels	0	<b>20.14</b>	<b>0.78</b>	<b>0.2942</b>	<b>3.4936</b>
30 pixels (Ours)	0.117	19.92	0.78	0.3031	3.7686
60 pixels	0.234	19.62	0.76	0.3225	3.8819
90 pixels	0.351	19.42	0.76	0.3107	3.9891
120 pixels	0.468	18.45	0.73	0.3442	4.1253

Table 3: Comparison of different misalignment pixels on real-world smoke dataset with  $256 \times 256$  size.

**Effect of non-aligned scales.** We redesign the real-world smoke dataset by considering the misalignment from 0 to 120 pixels. Table 3 reports the model performance (*i.e.*, PSNR, SSIM, FADE, and NIQE) with different non-aligned scales. These results show that the less misalignment, the better result. In this paper, we do the experiments on the smoke dataset with 30 pixels of misalignment, while the Phone-Hazy dataset has more than 30 pixels of misalignment, inconsistent focal length, and view.

**Effect of the various losses of  $\mathcal{L}_{msr}$  in Eq. (2) and  $\mathcal{L}_{rec}$  in Eq. (12).** Since  $\mathcal{L}_{msr}$  and  $\mathcal{L}_{rec}$  consist of  $\mathcal{L}_{adv}$ ,  $\mathcal{L}_{con}$ , and  $\mathcal{L}_1$ ,  $\mathcal{L}_p$ ,  $\mathcal{L}_{ssim}$ , respectively. Here, we separate these various losses to train our model on the real-world smoke dataset. The quantitative results are shown in Table 4. The up table shows the effectiveness of  $\mathcal{L}_{adv}$  and  $\mathcal{L}_{con}$ . In particular,  $\mathcal{L}_{adv+con}$  achieves a better performance than  $\mathcal{L}_{adv}$  and  $\mathcal{L}_{con}$  when fixed the loss  $\mathcal{L}_{rec}$ . The down table also showcases the similar effectiveness of  $\mathcal{L}_1$ ,  $\mathcal{L}_p$  and  $\mathcal{L}_{ssim}$ . In conclusion, these ablations demonstrate that these losses are useful to restore more details and improve the performance of image dehazing in real-world scenes.

## 5. Discussions

**Why do the dehazing results look blurry in the real world?** One plausible reason is that the hazy image has been degraded after particle scattering when it was captured by the camera [40]. But most of the models only consider the dehazing task and ignore the restoration. So, compared to the reference image, the dehazing results are blurred in real scenes. In contrast, the results of the synthetic data are better since the synthetic data are obtained by adding haze on a clear image, which does not change the sharpness of the image itself. Please see the visualization of dehazing

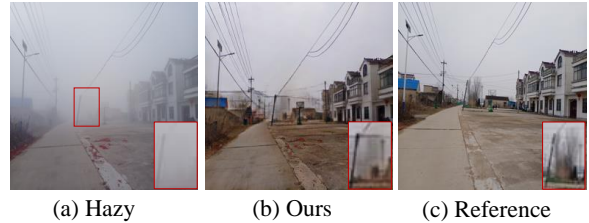


Figure 8: Failures of restoring the objects, which are occluded by dense haze in the far distance.

Fix $\mathcal{L}_{\ell_1} : \mathcal{L}_p : \mathcal{L}_{ssim}$ to 5 : 1 : 1				
$\mathcal{L}_{msr}$	PSNR $\uparrow$	SSIM $\uparrow$	FADE $\downarrow$	NIQE $\downarrow$
$\mathcal{L}_{adv}$	17.08	0.58	0.3328	3.8936
$\mathcal{L}_{con}$	18.04	0.76	0.3146	3.8037
$\mathcal{L}_{adv+con}$ (Ours)	<b>19.92</b>	<b>0.78</b>	<b>0.3031</b>	<b>3.7686</b>
Fix $\mathcal{L}_{adv} : \mathcal{L}_{con}$ to 1 : 1				
$\mathcal{L}_{rec}$	PSNR $\uparrow$	SSIM $\uparrow$	FADE $\downarrow$	NIQE $\downarrow$
$\mathcal{L}_{\ell_1}(base)$	19.11	0.76	0.3173	3.8168
$\mathcal{L}_{\ell_1+p}$	19.36	0.77	0.3158	3.7710
$\mathcal{L}_{\ell_1+p+ssim}$ (Ours)	<b>19.92</b>	<b>0.78</b>	<b>0.3031</b>	<b>3.7686</b>

Table 4: Ablation study for different loss items on real-world smoke dataset for  $\mathcal{L}_{msr}$  and  $\mathcal{L}_{rec}$ , respectively.

results for synthetic data in *the supplementary material*.

**Is SA is better than our mvSA for the non-uniform  $A_\infty$ ?**

No. The reason is that SA often outputs the attention map which shows many ineffective areas of  $A_\infty$ , while mvSA employs the DCP strategy to select the top 1% value points of the attention map to compute its mean. An example is shown in *the supplementary material*.

**Limitation.** Here, we discuss the limitation of our non-aligned dehazing framework. Dense haze is a challenging case, resulting in the dehazing CNN network being difficult to extract the meaningful feature because the network input does not contain any useful information except the thick haze. Therefore, our model may generate a few artifacts in the dehazing results. For example, in Fig 8, the dehazing results marked by the red boxes are not satisfactory and produce artifacts. For more discussions about our model, *please refer to the supplementary material*.

## 6. Conclusion

We have presented a novel and effective dehazing framework for real-world images that uses non-aligned supervision. This framework leverages a multi-scale reference loss to compare the prediction of the dehazing network with a clear and non-aligned reference image. It enables the collection of hazy/clear image pairs from real-world environments, even when they are not perfectly aligned. Additionally, our framework includes a mvSA network that uses dark channel prior to improve the estimation of the mean and variation of the airlight. The effectiveness of our framework was demonstrated through extensive experiments, which showed that it outperforms state-of-the-art methods in dehazing real-world images.



## References

- [1] Dana Berman, Shai Avidan, et al. Non-local image dehazing. In *Proceedings of the IEEE conference on computer vision and pattern recognition*, pages 1674–1682, 2016. [2](#)
- [2] Mario Bijelic, Tobias Gruber, Fahim Mannan, Florian Kraus, Werner Ritter, Klaus Dietmayer, and Felix Heide. Seeing through fog without seeing fog: Deep multimodal sensor fusion in unseen adverse weather. In *Proceedings of the IEEE/CVF Conference on Computer Vision and Pattern Recognition*, pages 11682–11692, 2020. [1](#)
- [3] Bolun Cai, Xiangmin Xu, Kui Jia, Chunmei Qing, and Dacheng Tao. Dehazenet: An end-to-end system for single image haze removal. *IEEE Transactions on Image Processing*, 25(11):5187–5198, 2016. [2](#), [12](#)
- [4] Xiang Chen, Zhentao Fan, Zhuoran Zheng, Yufeng Li, Yufeng Huang, Longgang Dai, Caihua Kong, and Pengpeng Li. Unpaired deep image dehazing using contrastive disentanglement learning. In *Proceedings of the european conference on computer vision (ECCV)*, 2022. [1](#), [5](#), [6](#), [12](#)
- [5] Zeyuan Chen, Yangchao Wang, Yang Yang, and Dong Liu. Psd: Principled synthetic-to-real dehazing guided by physical priors. In *Proceedings of the IEEE/CVF Conference on Computer Vision and Pattern Recognition*, pages 7180–7189, 2021. [1](#), [3](#), [5](#), [6](#), [12](#)
- [6] Lark Kwon Choi, Jaehee You, and Alan Conrad Bovik. Referenceless prediction of perceptual fog density and perceptual image defogging. *IEEE Transactions on Image Processing*, 24(11):3888–3901, 2015. [6](#)
- [7] Felipe Codevilla, Eder Santana, Antonio M López, and Adrien Gaidon. Exploring the limitations of behavior cloning for autonomous driving. In *Proceedings of the IEEE/CVF International Conference on Computer Vision*, pages 9329–9338, 2019. [1](#)
- [8] Xiaofeng Cong, Jie Gui, Kai-Chao Miao, Jun Zhang, Bing Wang, and Peng Chen. Discrete haze level dehazing network. In *Proceedings of the 28th ACM International Conference on Multimedia*, pages 1828–1836, 2020. [2](#)
- [9] Marius Cordts, Mohamed Omran, Sebastian Ramos, Timo Rehfeld, Markus Enzweiler, Rodrigo Benenson, Uwe Franke, Stefan Roth, and Bernt Schiele. The cityscapes dataset for semantic urban scene understanding. In *Proceedings of the IEEE conference on computer vision and pattern recognition*, pages 3213–3223, 2016. [2](#), [12](#)
- [10] Qili Deng, Ziling Huang, Chung-Chi Tsai, and Chia-Wen Lin. Hardgan: A haze-aware representation distillation gan for single image dehazing. In *European Conference on Computer Vision*, pages 722–738. Springer, 2020. [2](#)
- [11] Zijun Deng, Lei Zhu, Xiaowei Hu, Chi-Wing Fu, Xuemiao Xu, Qing Zhang, Jing Qin, and Pheng-Ann Heng. Deep multi-model fusion for single-image dehazing. In *Proceedings of the IEEE/CVF International Conference on Computer Vision*, pages 2453–2462, 2019. [2](#)
- [12] Hang Dong, Jinshan Pan, Lei Xiang, Zhe Hu, Xinyi Zhang, Fei Wang, and Ming-Hsuan Yang. Multi-scale boosted dehazing network with dense feature fusion. In *Proceedings of the IEEE/CVF Conference on Computer Vision and Pattern Recognition*, pages 2157–2167, 2020. [1](#), [2](#), [14](#)
- [13] Yu Dong, Yihao Liu, He Zhang, Shifeng Chen, and Yu Qiao. Fd-gan: Generative adversarial networks with fusion-discriminator for single image dehazing. *Proceedings of the AAAI Conference on Artificial Intelligence*, 34(07):10729–10736, 2020. [2](#)
- [14] Deniz Engin, Anil Genç, and Hazim Kemal Ekenel. Cycle-dehaze: Enhanced cyclegan for single image dehazing. In *Proceedings of the IEEE Conference on Computer Vision and Pattern Recognition Workshops*, pages 825–833, 2018. [3](#)
- [15] Raanan Fattal. Dehazing using color-lines. *ACM transactions on graphics (TOG)*, 34(1):1–14, 2014. [2](#)
- [16] Ian Goodfellow, Jean Pouget-Abadie, Mehdi Mirza, Bing Xu, David Warde-Farley, Sherjil Ozair, Aaron Courville, and Yoshua Bengio. Generative adversarial nets. *Advances in neural information processing systems*, 27, 2014. [4](#)
- [17] Chun-Le Guo, Qixin Yan, Saeed Anwar, Runmin Cong, Wenqi Ren, and Chongyi Li. Image dehazing transformer with transmission-aware 3d position embedding. In *Proceedings of the IEEE/CVF Conference on Computer Vision and Pattern Recognition*, pages 5812–5820, 2022. [2](#), [12](#), [14](#)
- [18] Martin Hahner, Christos Sakaridis, Dengxin Dai, and Luc Van Gool. Fog simulation on real lidar point clouds for 3d object detection in adverse weather. In *Proceedings of the IEEE/CVF International Conference on Computer Vision (ICCV)*, pages 15283–15292, October 2021. [1](#)
- [19] Kaiming He, Jian Sun, and Xiaoou Tang. Single image haze removal using dark channel prior. *IEEE transactions on pattern analysis and machine intelligence*, 33(12):2341–2353, 2010. [2](#), [3](#), [4](#), [5](#), [6](#), [12](#)
- [20] Kaiming He, Xiangyu Zhang, Shaoqing Ren, and Jian Sun. Deep residual learning for image recognition. In *Proceedings of the IEEE conference on computer vision and pattern recognition*, pages 770–778, 2016. [5](#)
- [21] Quan Huynh-Thu and Mohammed Ghanbari. Scope of validity of psnr in image/video quality assessment. *Electronics letters*, 44(13):800–801, 2008. [6](#)
- [22] Eunsung Jo and Jae-Young Sim. Multi-scale selective residual learning for non-homogeneous dehazing. In *Proceedings of the IEEE/CVF Conference on Computer Vision and Pattern Recognition*, pages 507–515, 2021. [1](#)
- [23] Justin Johnson, Alexandre Alahi, and Li Fei-Fei. Perceptual losses for real-time style transfer and super-resolution. In *European conference on computer vision*, pages 694–711. Springer, 2016. [2](#), [5](#)
- [24] Aupendu Kar, Sobhan Kanti Dhara, Debashis Sen, and Prabir Kumar Biswas. Transmission map and atmospheric light guided iterative updater network for single image dehazing. *arXiv preprint arXiv:2008.01701*, 2020. [2](#), [14](#)
- [25] Diederik P Kingma and Jimmy Ba. Adam: A method for stochastic optimization. *iclr*. 2015. *arXiv preprint arXiv:1412.6980*, 9, 2015. [6](#)
- [26] Boyi Li, Xiulian Peng, Zhangyang Wang, Jizheng Xu, and Dan Feng. Aod-net: All-in-one dehazing network. In *Proceedings of the IEEE international conference on computer vision*, pages 4770–4778, 2017. [2](#), [12](#)

- [27] Boyi Li, Wenqi Ren, Dengpan Fu, Dacheng Tao, Dan Feng, Wenjun Zeng, and Zhangyang Wang. Benchmarking single-image dehazing and beyond. *IEEE Transactions on Image Processing*, 28(1):492–505, 2018. 2, 6, 12
- [28] Ruoteng Li, Loong-Fah Cheong, and Robby T Tan. Heavy rain image restoration: Integrating physics model and conditional adversarial learning. In *Proceedings of the IEEE/CVF Conference on Computer Vision and Pattern Recognition*, pages 1633–1642, 2019. 2, 5
- [29] Runde Li, Jinshan Pan, Zechao Li, and Jinhui Tang. Single image dehazing via conditional generative adversarial network. In *Proceedings of the IEEE Conference on Computer Vision and Pattern Recognition*, pages 8202–8211, 2018. 2
- [30] Yi Li, Yi Chang, Yan Gao, Changfeng Yu, and Luxin Yan. Physically disentangled intra-and inter-domain adaptation for varicolored haze removal. In *Proceedings of the IEEE/CVF Conference on Computer Vision and Pattern Recognition*, pages 5841–5850, 2022. 2
- [31] Yunan Li, Qiguang Miao, Wanli Ouyang, Zhenxin Ma, Huijuan Fang, Chao Dong, and Yining Quan. Lap-net: Level-aware progressive network for image dehazing. In *Proceedings of the IEEE/CVF International Conference on Computer Vision*, pages 3276–3285, 2019. 2
- [32] Huan Liu, Zijun Wu, Liangyan Li, Sadaf Salehkalibar, Jun Chen, and Keyan Wang. Towards multi-domain single image dehazing via test-time training. In *Proceedings of the IEEE/CVF Conference on Computer Vision and Pattern Recognition*, pages 5831–5840, 2022. 2
- [33] Wei Liu, Fei Zhou, Tao Lu, Jiang Duan, and Guoping Qiu. Image defogging quality assessment: Real-world database and method. *IEEE Transactions on image processing*, 30:176–190, 2020. 12
- [34] Xiaohong Liu, Yongrui Ma, Zhihao Shi, and Jun Chen. Grid-dehazenet: Attention-based multi-scale network for image dehazing. In *Proceedings of the IEEE/CVF International Conference on Computer Vision*, pages 7314–7323, 2019. 2
- [35] Yang Liu, Jinshan Pan, Jimmy Ren, and Zhixun Su. Learning deep priors for image dehazing. In *Proceedings of the IEEE/CVF International Conference on Computer Vision*, pages 2492–2500, 2019. 2, 5
- [36] Earl J McCartney. Optics of the atmosphere: scattering by molecules and particles. *New York*, 1976. 2
- [37] Roey Mechrez, Itamar Talmi, and Lihi Zelnik-Manor. The contextual loss for image transformation with non-aligned data. In *Proceedings of the European conference on computer vision (ECCV)*, pages 768–783, 2018. 4
- [38] Anish Mittal, Rajiv Soundararajan, and Alan C Bovik. Making a “completely blind” image quality analyzer. *IEEE Signal processing letters*, 20(3):209–212, 2012. 6
- [39] Ranjan Mondal, Sanchayan Santra, and Bhabatosh Chanda. Image dehazing by joint estimation of transmittance and airlight using bi-directional consistency loss minimized fcn. In *Proceedings of the IEEE Conference on Computer Vision and Pattern Recognition Workshops*, pages 920–928, 2018. 2
- [40] Shree K Nayar and Srinivasa G Narasimhan. Vision in bad weather. In *Proceedings of the Seventh IEEE International Conference on Computer Vision*, volume 2, pages 820–827. IEEE, 1999. 8
- [41] Yanwei Pang, Jing Nie, Jin Xie, Jungong Han, and Xuelong Li. Bidnet: Binocular image dehazing without explicit disparity estimation. In *Proceedings of the IEEE/CVF Conference on Computer Vision and Pattern Recognition*, pages 5931–5940, 2020. 2
- [42] Jaihyun Park, David K Han, and Hanseok Ko. Fusion of heterogeneous adversarial networks for single image dehazing. *IEEE Transactions on Image Processing*, 29:4721–4732, 2020. 2
- [43] Xu Qin, Zhilin Wang, Yuanchao Bai, Xiaodong Xie, and Huizhu Jia. Ffa-net: Feature fusion attention network for single image dehazing. *Proceedings of the AAAI Conference on Artificial Intelligence*, 34(07):11908–11915, 2020. 2, 12, 14
- [44] Yanyun Qu, Yizi Chen, Jingying Huang, and Yuan Xie. Enhanced pix2pix dehazing network. In *Proceedings of the IEEE/CVF Conference on Computer Vision and Pattern Recognition*, pages 8160–8168, 2019. 2, 12
- [45] Wenqi Ren, Si Liu, Hua Zhang, Jinshan Pan, Xiaochun Cao, and Ming-Hsuan Yang. Single image dehazing via multi-scale convolutional neural networks. In *European conference on computer vision*, pages 154–169. Springer, 2016. 2, 12
- [46] Wenqi Ren, Lin Ma, Jiawei Zhang, Jinshan Pan, Xiaochun Cao, Wei Liu, and Ming-Hsuan Yang. Gated fusion network for single image dehazing. In *Proceedings of the IEEE Conference on Computer Vision and Pattern Recognition*, pages 3253–3261, 2018. 2
- [47] Olaf Ronneberger, Philipp Fischer, and Thomas Brox. U-net: Convolutional networks for biomedical image segmentation. In *International Conference on Medical image computing and computer-assisted intervention*, pages 234–241. Springer, 2015. 3, 4
- [48] Christos Sakaridis, Dengxin Dai, Simon Hecker, and Luc Van Gool. Model adaptation with synthetic and real data for semantic dense foggy scene understanding. In *Proceedings of the european conference on computer vision (ECCV)*, pages 687–704, 2018. 1
- [49] Yuanjie Shao, Lerenhan Li, Wenqi Ren, Changxin Gao, and Nong Sang. Domain adaptation for image dehazing. In *Proceedings of the IEEE/CVF Conference on Computer Vision and Pattern Recognition*, pages 2808–2817, 2020. 1, 2, 3, 5, 6
- [50] Pranjay Shyam, Kuk-Jin Yoon, and Kyung-Soo Kim. Towards domain invariant single image dehazing. In *Proceedings of the AAAI Conference on Artificial Intelligence*, volume 35, pages 9657–9665, 2021. 2
- [51] Yuda Song, Zhuqing He, Hui Qian, and Xin Du. Vision transformers for single image dehazing. *arXiv preprint arXiv:2204.03883*, 2022. 2
- [52] Robby T Tan. Visibility in bad weather from a single image. In *2008 IEEE Conference on Computer Vision and Pattern Recognition*, pages 1–8. IEEE, 2008. 2
- [53] Jeya Maria Jose Valanarasu, Rajeev Yasarla, and Vishal M Patel. Transweather: Transformer-based restoration of images degraded by adverse weather conditions. In *Proceed-*

- ings of the *IEEE/CVF Conference on Computer Vision and Pattern Recognition*, pages 2353–2363, 2022. 2
- [54] Kun Wang, Zhenyu Zhang, Zhiqiang Yan, Xiang Li, Baobei Xu, Jun Li, and Jian Yang. Regularizing nighttime weirdness: Efficient self-supervised monocular depth estimation in the dark. In *Proceedings of the IEEE/CVF International Conference on Computer Vision*, pages 16055–16064, 2021. 1
- [55] Xiaolong Wang, Ross Girshick, Abhinav Gupta, and Kaiming He. Non-local neural networks. In *Proceedings of the IEEE conference on computer vision and pattern recognition*, pages 7794–7803, 2018. 4
- [56] Zhou Wang, Alan C Bovik, Hamid R Sheikh, and Eero P Simoncelli. Image quality assessment: from error visibility to structural similarity. *IEEE transactions on image processing*, 13(4):600–612, 2004. 5, 6
- [57] Haiyan Wu, Yanyun Qu, Shaohui Lin, Jian Zhou, Ruizhi Qiao, Zhizhong Zhang, Yuan Xie, and Lizhuang Ma. Contrastive learning for compact single image dehazing. In *Proceedings of the IEEE/CVF Conference on Computer Vision and Pattern Recognition*, pages 10551–10560, 2021. 1, 12
- [58] Qingbo Wu, Jingang Zhang, Wenqi Ren, Wangmeng Zuo, and Xiaoqun Cao. Accurate transmission estimation for removing haze and noise from a single image. *IEEE Transactions on Image Processing*, 29:2583–2597, 2019. 2
- [59] Xitong Yang, Zheng Xu, and Jiebo Luo. Towards perceptual image dehazing by physics-based disentanglement and adversarial training. *Proceedings of the AAAI Conference on Artificial Intelligence*, 32(1), 2018. 3, 5, 6, 12
- [60] Yang Yang, Chaoyue Wang, Risheng Liu, Lin Zhang, Xiaojie Guo, and Dacheng Tao. Self-augmented unpaired image dehazing via density and depth decomposition. In *Proceedings of the IEEE/CVF Conference on Computer Vision and Pattern Recognition*, pages 2037–2046, 2022. 1, 5, 6, 12
- [61] Tian Ye, Mingchao Jiang, Yunchen Zhang, Liang Chen, Erkang Chen, Pen Chen, and Zhiyong Lu. Perceiving and modeling density is all you need for image dehazing. In *Proceedings of the european conference on computer vision (ECCV)*, 2022. 2, 14
- [62] Tian Ye, Yun Liu, Yunchen Zhang, Sixiang Chen, and Erkang Chen. Mutual learning for domain adaptation: Self-distillation image dehazing network with sample-cycle. *arXiv preprint arXiv:2203.09430*, 2022. 2
- [63] Hu Yu, Jie Huang, Yajing Liu, Qi Zhu, Man Zhou, and Feng Zhao. Source-free domain adaptation for real-world image dehazing. In *Proceedings of the 30th ACM International Conference on Multimedia*, pages 6645–6654, 2022. 2
- [64] He Zhang and Vishal M Patel. Densely connected pyramid dehazing network. In *Proceedings of the IEEE conference on computer vision and pattern recognition*, pages 3194–3203, 2018. 2, 5
- [65] He Zhang, Vishwanath Sindagi, and Vishal M Patel. Joint transmission map estimation and dehazing using deep networks. *IEEE Transactions on Circuits and Systems for Video Technology*, 30(7):1975–1986, 2019. 2
- [66] Dong Zhao, Jia Li, Hongyu Li, and Long Xu. Hybrid local-global transformer for image dehazing. *arXiv preprint arXiv:2109.07100*, 2021. 2
- [67] Shiyu Zhao, Lin Zhang, Shuaiyi Huang, Ying Shen, Shengjie Zhao, and Yukai Yang. Evaluation of defogging: A real-world benchmark dataset, a new criterion and baselines. In *2019 IEEE international conference on multimedia and expo (ICME)*, pages 1840–1845. IEEE, 2019. 12
- [68] Shiyu Zhao, Lin Zhang, Ying Shen, and Yicong Zhou. Refinednet: A weakly supervised refinement framework for single image dehazing. *IEEE Transactions on Image Processing*, 30:3391–3404, 2021. 1, 3, 5, 6, 12
- [69] Zhuoran Zheng, Wenqi Ren, Xiaoqun Cao, Xiaobin Hu, Tao Wang, Fenglong Song, and Xiuyi Jia. Ultra-high-definition image dehazing via multi-guided bilateral learning. In *2021 IEEE/CVF Conference on Computer Vision and Pattern Recognition (CVPR)*, pages 16180–16189. IEEE, 2021. 1, 14
- [70] Chu Zhou, Mingguo Teng, Yufei Han, Chao Xu, and Boxin Shi. Learning to dehaze with polarization. *Advances in Neural Information Processing Systems*, 34:11487–11500, 2021. 2
- [71] Jun-Yan Zhu, Taesung Park, Phillip Isola, and Alexei A Efros. Unpaired image-to-image translation using cycle-consistent adversarial networks. In *Proceedings of the IEEE international conference on computer vision*, pages 2223–2232, 2017. 3
- [72] Qingsong Zhu, Jiaming Mai, and Ling Shao. A fast single image haze removal algorithm using color attenuation prior. *IEEE transactions on image processing*, 24(11):3522–3533, 2015. 2

## S. Supplementary Material

This supplementary material consists of the following seven parts: Phone-Hazy dataset collection setting (S.1), Test our model on hazy video (S.2), the experimental results on two synthetic datasets (S.3), the detailed structure of shared network (S.4), additional ablation study (S.5), additional discussion (S.6), and additional quantitative and visual results (S.7).

### S.1. Phone-Hazy Dataset Collection Setting

To collect pairs of hazy/clear image pairs, follow these steps: 1. Capture hazy images using a mobile phone (iphone XR) on a hazy day, preferably focusing on buildings to avoid interference from vehicles and pedestrians. 2. Take a clean reference image of the same scene under cloudy conditions, based on the foggy image. 3. Preprocess the hazy/clear image pairs (e.g., crop) to maintain their semantic consistency as much as possible, even if minor inconsistencies won't have a significant impact. This makes data collection more convenient in real scene. An example pair of images is shown below:



Figure S1: An example of hazy/clear image pairs for Phone-Hazy dataset.

Compared to the 208 image pairs in the BeDDE [67] dataset, our Phone-Hazy dataset contains a larger volume of data and more diverse scenes, and the feature similarity between our haze and reference images is higher. Additionally, while the MRFID [33] dataset has a large volume of data, its scenes are relatively uniform, consisting mainly of mountains.

### S.2. Test on Hazy Video

To verify the practicality of our dehazing model in real-world scenarios, we tested it on real hazy videos with varying concentrations. Results showed that our model performed well in handling hazy video data and exhibited good stability in multi-frame consistency (i.e., the brightness and color of scene). For the visual results, please refer to the .mp4 file included in the supplementary materials.

### S.3. Experiments on Synthetic Dataset

**SOTS dataset.** For SOTS dataset, we choose 6000 synthetic hazy images from training, 3000 from ITS and 3000 from OTS. SOTS is used for test, which contains 500 indoor hazy images and 500 outdoor hazy ones. Here, ITS, OTS

Methods	SOTS		Foggy Cityscapes		Reference
	PSNR $\uparrow$	SSIM $\uparrow$	PSNR $\uparrow$	SSIM $\uparrow$	
DCP [19]	15.49	0.65	16.51*	0.73*	CVPR'09
DisentGAN [59]	21.48*	0.84*	25.49*	0.92*	AAAI'18
MSCNN [45]	17.57	0.81	18.99	0.86	ECCV'16
DehazeNet [3]	21.14	0.85	14.97	0.49	TIP'16
AOD-Net [26]	19.06	0.85	15.45	0.63	ICCV'17
EPDN [44]	23.82	0.89	25.23*	0.94*	CVPR'19
AECR-Net [57]	<b>37.17</b>	<b>0.99</b>	-	-	CVPR'21
PSD [5]	12.17*	0.64*	11.16*	0.55*	CVPR'21
RefineNet [68]	24.39	0.91	23.54*	0.93*	TIP'21
CDD-GAN [4]	24.61	0.92	24.72*	0.90*	ECCV'22
<b>NSDNet (Ours)</b>	25.02	0.92	<b>29.35</b>	<b>0.96</b>	-

Table S1: Quantitative comparison (average PSNR/SSIM) of the dehazing results on SOTS (indoor & outdoor) dataset and Foggy Cityscapes dataset.  $\uparrow$  represents the higher the better. The symbol "\*" means that we finetune the model on the Foggy Cityscapes train set.

Methods	Dense-Haze		NH-HAZE		Reference
	PSNR $\uparrow$	SSIM $\uparrow$	PSNR $\uparrow$	SSIM $\uparrow$	
FFANet [43]	12.22	0.4440	18.13	0.6473	AAAI'20
AECR-Net [57]	15.80	0.4660	19.88	0.7173	CVPR'21
DeHamer [17]	16.62	<b>0.5602</b>	20.66	0.6844	CVPR'22
<b>NSDNet(Ours)</b>	<b>16.73</b>	0.5304	<b>20.68</b>	<b>0.7209</b>	-
	SOTS-indoor		SOTS-outdoor		
FFANet [43]	36.39	<b>0.9886</b>	20.23	0.905	AAAI'20
D <sup>4</sup> [60]	25.42	0.932	25.83	0.956	CVPR'22
DeHamer [17]	<b>36.63</b>	0.9881	<b>35.18</b>	<b>0.9860</b>	CVPR'22
<b>NSDNet(Ours)</b>	26.47	0.936	27.49	0.9282	-

Table S2: Quantitative comparison of the dehazing results on Dense-Haze, NH-HAZE, SOTS-indoor and SOTS-outdoor dataset.

and SOTS are three subsets of the RESIDE [27] dataset, respectively.

**Foggy Cityscapes dataset**<sup>1</sup>. The Foggy cityscapes dataset [9] is a binocular foggy image pairs dataset. In this work, we use a monocular part of the datasets, i.e., left image. there are 8,925 monocular hazy/clear image pairs in training set, 1500 monocular hazy/clear image pairs in validation set for the Foggy Cityscapes dataset.

To further verify the effectiveness of our proposed method, we evaluate the proposed method against SOTA methods that require aligned ground truths. Table S1 reports the evaluation results on the SOTS dataset and Foggy Cityscapes dataset in terms of PSNR and SSIM. We can see that our proposed method obtains higher PSNR and SSIM values than the state-of-the-art (SOTA) methods on Foggy Cityscapes dataset. In this work, we mainly focus on the real image dehazing. Table S2 demonstrates that our method does not achieves the SOTA results on SOTS dataset, but

<sup>1</sup><https://www.cityscapes-dataset.com/>

Shared Network			
layers	setting	input	output
pre-processing	3x3, 64, s=1 3x3, 64, s=1	256x256x3	256x256x64
down_sample_1	3x3, 128, s=2	256x256x64	128x128x128
down_sample_2	3x3, 256, s=2	128x128x128	64x64x256
down_sample_3	3x3, 512, s=2	64x64x256	32x32x512
down_sample_4	3x3, 1024, s=2	32x32x512	16x16x1024
up_sample_4	$\left[ \begin{array}{l} \text{upsample, s=2} \\ 3x3, 512, s=2 \\ \oplus \text{ up\_sample\_3} \end{array} \right]$	16x16x1024	32x32x512
up_sample_3	$\left[ \begin{array}{l} \text{upsample, s=2} \\ 3x3, 256, s=2 \\ \oplus \text{ up\_sample\_2} \end{array} \right]$	32x32x512	64x64x256
up_sample_2	$\left[ \begin{array}{l} \text{upsample, s=2} \\ 3x3, 128, s=2 \\ \oplus \text{ up\_sample\_1} \end{array} \right]$	64x64x256	128x128x128
up_sample_1	3x3, 64, s=2	128x128x128	256x256x64

Table S3: The detailed architecture of the shared network for feature extraction.  $\oplus$  denotes the concatenation operation.

we achieved the best dehazing performance on Dense-Haze and NH-HAZE datasets.

We further present visual observation comparisons in Fig. S2. The dehazing results of all the competitive methods contain artifacts, and the detail restoration are not ideal. In contrast, the proposed method generates much clearer results that are visually closer to the ground truth. *More visual results are shown in Figs. S11-S13*

#### S.4. Structure of Shared Network

The shared feature extraction network is an encoder-decoder structure with skip connection, and the detailed structure is shown in Table S3.

#### S.5. Additional Ablation Study

**Effect of scale selection for  $\mathcal{L}_{\text{msr}}$ .** The proposed  $\mathcal{L}_{\text{msr}}$  contains different scales. We further evaluate the effect of the different scales by setting three scales ( $0.5\times$ ,  $1\times$ ,  $2\times$ ). Table S4 shows that multi-scale can help improve the performance of  $\mathcal{L}_{\text{msr}}$ . We empirically use three scales ( $0.5\times$ ,  $1\times$ ,  $2\times$ ) as a trade-off between performance and computational complexity.

The scale of $\mathcal{L}_{\text{msr}}$	$0.5\times$	$1\times$	$2\times$	FADE $\downarrow$	NIQE $\downarrow$
$1\times$		✓		0.7921	4.1225
$0.5\times$ & $1\times$	✓	✓		0.8043	3.9782
$1\times$ & $2\times$		✓	✓	0.7786	4.3201
$0.5\times$ & $1\times$ & $2\times$ (Ours)	✓	✓	✓	<b>0.7621</b>	<b>3.7884</b>

Table S4: Comparison of different scales on real-world Phone-Hazy dataset for  $\mathcal{L}_{\text{msr}}$ . & denotes "and".

#### S.6. Additional Discussion

In this section, we discuss two problems to better understand our model.

**Why our framework works ?** There are three explanations. 1) Our definitions of infinite airlight  $A_\infty$  and transmission map  $t$  are closer to the real scene. So, our  $A_\infty$  and  $t$  can generate dehazing results with better visual quality are shown in Fig. 6, thus producing a better restraint effect on dehazing result  $J$ . 2) We designed multi-scale reference loss to enable our framework more accurately recover the brightness and texture of haze-free scenes by referencing the non-aligned images of the corresponding scene. 3) Our framework is more reasonable and effective by constraints of physical priors.

**Which is better for transmission map  $t$ , single-channel or three-channel ?** According to  $t(x) = e^{-\beta(\lambda)d(x)}$ , in two cases, the  $t$  will tend to 0, one is the hazy area, another is the sky area at infinity (*i.e.*,  $d(x)$  tends to  $\infty$ ). From Fig. S3 (b), we can observe that the  $t$  of the white chair marked by the red box should not tend to 0 for single-channel  $t$ . In contrast, the three-channel  $t$  is relatively more accurate, and the dehazing results are also better.

**Regarding reference image rotation  $30^\circ$ ,  $60^\circ$  and  $90^\circ$ .** Table S5 shows results of rotating the non-aligned reference images by  $0\sim 30^\circ$  (simulate the real scene),  $60^\circ$  and  $90^\circ$  on real-world smoke, respectively. We have observed that the model is susceptible to variations in the rotation degree of the reference image, owing to the sensitivity of the contextual loss to pixel positions. Nevertheless, in the context of actual data acquisition, it is relatively straightforward to constrain the rotation degree of captured images to a range of  $0\sim 30$  degrees.

Rotation	$0\sim 30^\circ$ (Ours)	$30^\circ$	$60^\circ$	$90^\circ$
PSNR $\uparrow$	<b>18.74</b>	12.85	12.00	11.52
SSIM $\uparrow$	<b>0.76</b>	0.23	0.19	0.14

Table S5: Comparing reference images at different rotation degree on the real-world smoke dataset.

#### S.7. Additional Quantitative and Visual Results

We also provide additional visual results on synthetic dataset (*i.e.*, Foggy Cityscapes), real-world dataset (*e.g.*, real-world smoke, real-world Phone-Hazy and RTTS). Figs. S5-S6 are visual comparisons on real-world smoke dataset. The visual comparison of real-world Phone-Hazy dataset is shown in Figs. S7-S8. The quantitative results and visual comparison on RTTS dataset are presented in Table S6 and Figs. S9-S10, respectively.

**More comparison results on real-world smoke dataset.** The Figs. S5-S6 shows that the restored images of DCP, RefineNet and  $D^4$  are darker than the reference images, and cannot completely remove smoke in some regions. The DAD and PSD don't remove smoke well, and the



Figure S2: Comparison of dehazing results on synthetic hazy dataset.

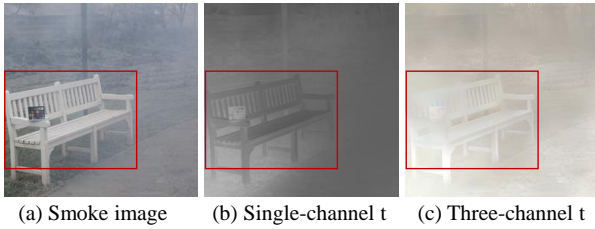


Figure S3: Comparison of single-channel and three-channel transmission map  $t$ .

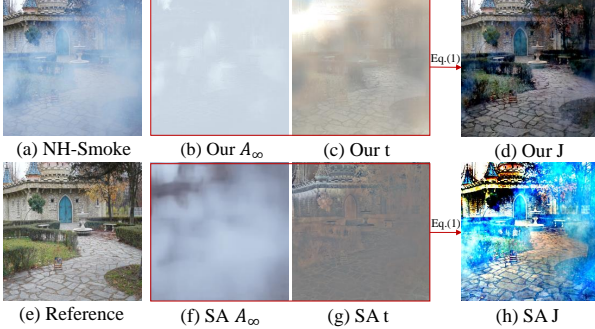


Figure S4: Visual comparison of  $A_\infty$ ,  $t$  and  $J$  of mvSA and SA.

Data Setting	Methods	RTTS (Only testing)		Reference
		FADE ↓	NIQE ↓	
Aligned ( <i>i.e.</i> , need GT)	MSBDN [12]	1.3952	4.5269	CVPR'20
	FFANet [43]	2.0734	4.9281	AAAI'20
	UHD [69]	1.2457	4.4244	CVPR'21
	IPUDN [24]	0.9126	7.3470	Arxiv'22
	PMNet [61]	1.4211	4.7523	ECCV'22
	Dehamer [17]	1.3062	7.2924	CVPR'22
Non-aligned	<b>NSDNet (Ours)</b>	<b>0.7419</b>	<b>3.6905</b>	-

Table S6: Comparison of the proposed method and methods with aligned ground truth on RTTS dataset.

dehazing results of PSD only seem to increase the bright-

ness of scenes. The dehazing results of DisentGAN are blurred. Though CDD-GAN has achieved a better visual than the above methods, the detail of restored images (*i.e.*, color, texture and brightness) is worse than our method in general. In contrast, our method can restore more natural haze-free images, which achieves a better visual quality.

**More comparison results on real-world Phone-Hazy dataset.** From Figs. S7-S8, we can observe that DCP, DisentGAN, PSD and  $D^4$  cannot successfully remove hazy in the far distance, and the restored results of DCP, PSD and  $D^4$  are lower than reference image in general. The DAD has a serious artifact in the sky area. The CDD-GAN can remove hazy in far distance, but the texture of dehazing results of CDD-GAN is more blurry than our results in detail. Compared with these methods, our method can remove hazy in the far distance and restore more details (*i.e.*, color and textures), which are closer to the reference image.

**More quantitative results and visual comparison on real-world RTTS dataset.** To verify the effectiveness of different methods in real hazy scenes, we employ RTTS dataset to test both classical and SOTA dehazing methods. As shown in Figs. S9-S10, RefineNet and UHD suffer from serious color distortions (*e.g.*, the sky area). The dehazing results by PSD,  $D^4$ , MSBDN, FFANet, IPUDN, PMNet and Dehamer still contain the haze residual. Though CDD-GAN has achieved a better visual effect than the above methods, the texture and color of the dehazing results are worse than our method in detail.



Figure S5: Comparison of dehazing results on real-world homogeneous smoke dataset.



Figure S6: Comparison of dehazing results on real-world non-homogeneous smoke dataset.



Figure S7: Comparison of dehazing results on real-world Phone-Hazy dataset.



Figure S8: Comparison of dehazing results on real-world Phone-Hazy dataset.



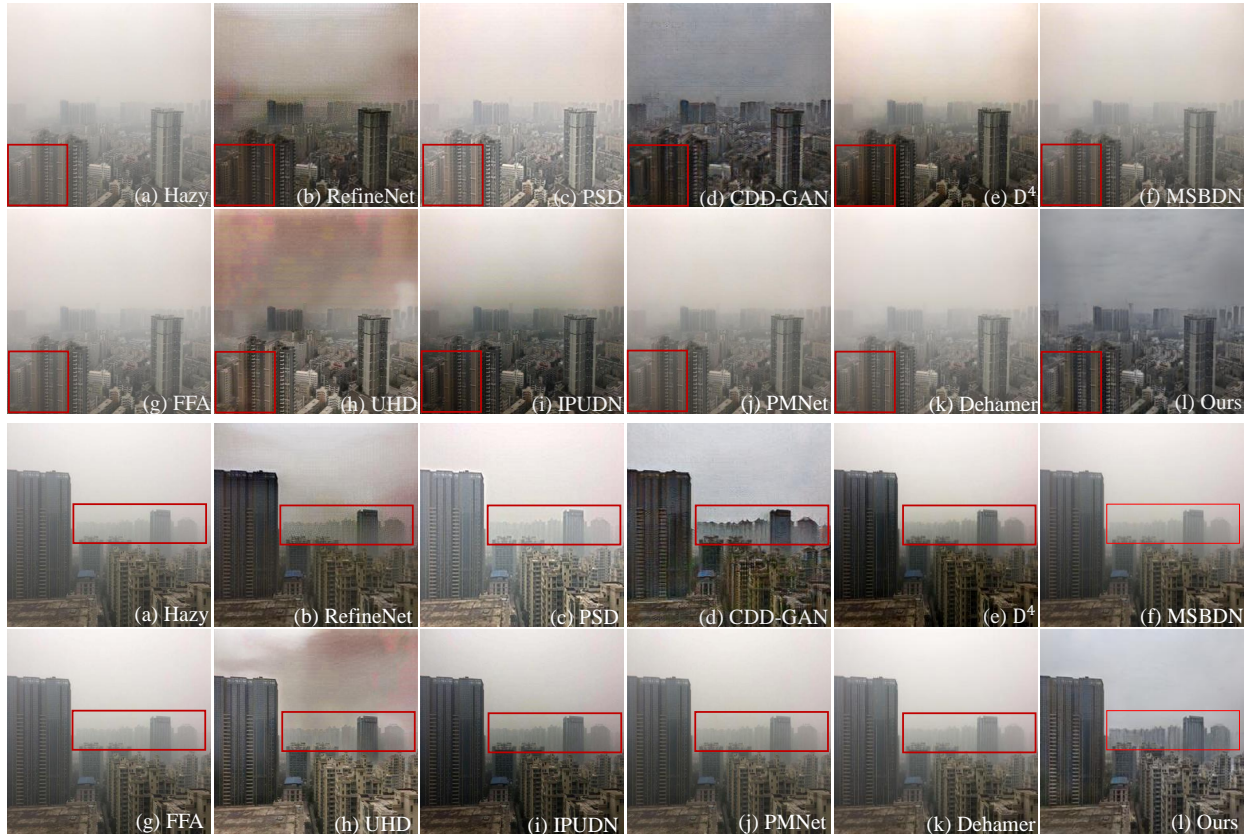


Figure S9: Comparison of dehazing results on RTTS dataset.

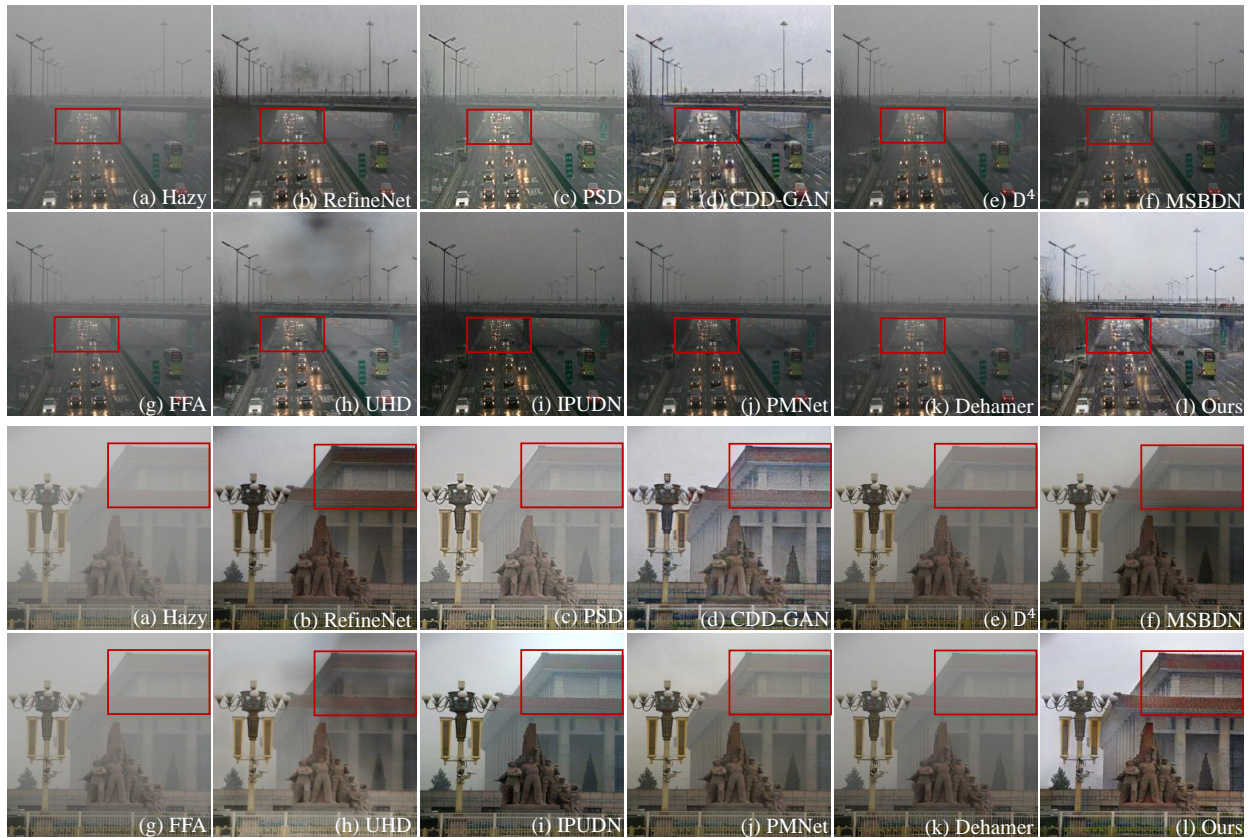


Figure S10: Comparison of dehazing results on RTTS dataset.

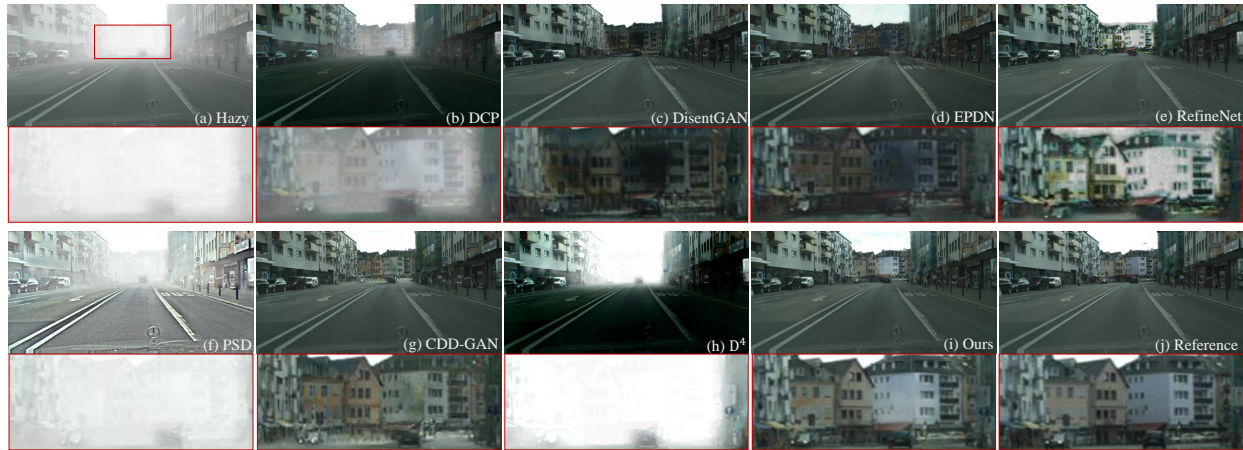


Figure S11: Comparison of dehazing results on Foggy Cityscapes dataset.



Figure S12: Comparison of dehazing results on Foggy Cityscapes dataset.



Figure S13: Comparison of dehazing results on Foggy Cityscapes dataset.